



CHEMICAL ABUNDANCES IN NGC 5024 (M53): A MOSTLY FIRST GENERATION GLOBULAR CLUSTER

OWEN M. BOBERG¹, EILEEN D. FRIEL¹, AND ENRICO VESPERINI

Astronomy Department, Indiana University, Bloomington, IN 47405, USA

Received 2016 January 27; accepted 2016 March 10; published 2016 June 3

ABSTRACT

We present the Fe, Ca, Ti, Ni, Ba, Na, and O abundances for a sample of 53 red giant branch stars in the globular cluster (GC) NGC 5024 (M53). The abundances were measured from high signal-to-noise medium resolution spectra collected with the Hydra multi-object spectrograph on the Wisconsin–Indiana–Yale–NOAO 3.5 m telescope. M53 is of interest because previous studies based on the morphology of the cluster’s horizontal branch suggested that it might be composed primarily of first generation (FG) stars and differ from the majority of other GCs with multiple populations, which have been found to be dominated by the second generation (SG) stars. Our sample has an average $[\text{Fe}/\text{H}] = -2.07$ with a standard deviation of 0.07 dex. This value is consistent with previously published results. The alpha-element abundances in our sample are also consistent with the trends seen in Milky Way halo stars at similar metallicities, with enhanced $[\text{Ca}/\text{Fe}]$ and $[\text{Ti}/\text{Fe}]$ relative to solar. We find that the Na–O anti-correlation in M53 is not as extended as other GCs with similar masses and metallicities. The ratio of SG to the total number of stars in our sample is approximately 0.27 and the SG generation is more centrally concentrated. These findings further support that M53 might be a mostly FG cluster and could give further insight into how GCs formed the light element abundance patterns we observe in them today.

Key words: Galaxy: abundances – globular clusters: individual (NGC 5024)

Supporting material: machine-readable tables

1. INTRODUCTION

The presence of light element anti-correlations has become a defining characteristic of Galactic globular clusters (GC). Through large systematic spectroscopic surveys (see, e.g., Gratton et al. 2012, and references therein), nearly all GCs have been found to exhibit a Na–O anti-correlation, except in only the least massive GCs (Carretta et al. 2010). High quality photometric surveys from the *Hubble Space Telescope* (Piotto et al. 2015), and other observatories, have also shown that these chemical inhomogeneities are expressed as multiple main sequences, broadened subgiant branches, and split red giant branches (RGB). These color–magnitude diagram (CMD) morphologies differ from what one would expect from a simple coeval and chemically homogeneous stellar population, suggesting that GCs have undergone a not-so-simple evolution.

Currently in the literature a variety of physical mechanisms have been suggested to produce the abundance patterns and CMD morphology observed in GCs. A number of these mechanisms involve the cluster undergoing a period of self-enrichment in which the processed gas from a first generation (FG) of evolved stars has polluted the interstellar medium in which a second generation (SG) eventually forms. Possible FG polluters include rapidly rotating massive stars, massive binary stars, and intermediate-mass AGB stars (see, e.g., Ventura et al. 2001; Prantzos & Charbonnel 2006; D’Ercole et al. 2008, 2010, 2012; de Mink et al. 2009). There are also proposed scenarios that do not require a second epoch of stars formation to produce the chemical signatures of the apparent SG (Bastian et al. 2013).

In those GCs that exhibit the Na–O anti-correlation, the SG is typically found to be the dominant population in the cluster, or at least equal in number to the FG (Carretta et al. 2009b).

This finding has given rise to what is known as the mass budget problem. The current number of FG stars in GCs is not large enough to provide enough processed gas to form the large fraction of SG stars that are observed today in GCs. In order to explain the lack of FG stars currently seen in GCs, it has been suggested that the natal mass of GCs is much larger than we observe today, and they have lost the majority of their FG stars through tidal interactions with the Galaxy and early cluster dynamical evolution.

It has been suggested in a number of studies (see, e.g., D’Ercole et al. 2008; Decressin et al. 2010) that such a large loss of FG stars might occur during early evolutionary stages as a result of the cluster expansion due to primordial gas expulsion and/or mass loss of SNII ejecta. For very compact and tidally underfilling clusters, however, such an expansion phase would not be efficient in removing a large fraction of FG stars and might leave the cluster with a fraction of SG stars close to the primordial one. Following this scenario, Caloi & D’Antona (2011) suggested that tidally underfilling FG-dominated clusters might exist. It is, however, important to point out that the current position of a cluster in the Galaxy and its current Galactic environment might be significantly different from the early environment in which the cluster evolved during the early FG loss phase. A present-day tidally underfilling structure therefore does not necessarily imply that the cluster must be dominated by FG stars. Caloi & D’Antona (2011) identified a number of Milky Way (MW) GCs as candidates to be FG-only or FG-dominated clusters based on their physical characteristics and the morphology of their horizontal branches (HB). NGC 5024 (M53) was one of the clusters they identified as a FG-dominated candidate. Table 1 gives some basic information on M53. Based on HB simulations of M53, Caloi & D’Antona (2011) conclude that the ratio of SG to FG stars in M53 is approximately 50/500, and the SG is more centrally concentrated in the cluster. They noted that this ratio is only approximate and needed additional photometric and

¹ Visiting Astronomer, Kitt Peak National Observatory, National Optical Astronomy Observatory, which is operated by the Association of Universities for Research in Astronomy, Inc. (AURA) under cooperative agreement with the National Science Foundation.

Table 1
NGC 5024 (M53) Properties

Cluster	R.A. (J2000)	Decl. (J2000)	(l, b)	R_{\odot}^a (kpc)	R_{GC}^a (kpc)	r_c^b (pc)	r_h^b (pc)	r_{tr}^b (pc)	$\log\left(\frac{r_{tr}}{r_c}\right)^c$
M53	13:12:55.24	+18:10:05.4	333°, 80°	17.9	18.4	2.18	5.84	239.9	2.04

Notes.

^a Harris (1996, Version 2010).

^b McLaughlin & van der Marel (2005).

spectroscopic follow up. CN and CH molecular band studies (see, e.g., Martell et al. 2008; Smolinski et al. 2011) have also shown that there are CN-strong and CN-weak populations in M53, but the sample sizes are too small to draw conclusions about their relative fractions in the cluster.

Also of interest are the results of wide-field photometric surveys of M53 and its neighboring GC NGC 5053. Using Megacam on the Canada–France–Hawaii Telescope, Chun et al. (2010) find extra-tidal features in both clusters, a tidal bridge-like structure between the two GCs, and an envelope over-density of stars around the pair. Using SDSS Jordi & Grebel (2010) did a similar wide-field study of the clusters, and do not find a tidal bridge-like structure between them.

In order to characterize the abundances in the multiple populations in M53, and add to the constraints on their relative fractions, we have collected high quality spectra for a large sample of RGB stars in the cluster. This is part of a comprehensive photometric, spectroscopic, and kinematic study of M53 and NGC 5053. Our findings regarding the abundances in NGC 5053 are published in Boberg et al. (2015).

In this paper we will present Fe, Ca, Ti, Ni, Ba, O, and Na abundances for the cluster members in our sample. We were able to determine the Na and O abundances in a large enough sample of stars, over a wide range of distances from the cluster center, to characterize the relative fraction of FG and SG stars in the cluster as well as their radial distributions. The sections of the paper are organized in the following order: In Section 2 we will present how we performed our observations, data reductions, and selected the science targets in M53. In Section 3 we will present how the abundance analysis was performed using both equivalent width (EW) measurements and spectral synthesis and the errors associated with the different measurements. In Section 4 we will present the results of the abundance analysis as well as a comparison of our results with other abundance measurements in the literature. In Section 5 we will discuss the extent of the Na–O anti-correlation, how we separated the stars into FG and SG, the radial distribution of each population, and how our results fit in with the CN and CH molecular band strength studies. We will conclude with a discussion of the implications of our results as well as future plans for photometric and dynamical studies of the cluster.

2. OBSERVATIONS AND DATA REDUCTION

2.1. Observations

The observations for this study were taken on the Wisconsin–Indiana–Yale–NOAO (WIYN) 3.5 m telescope²

² The WIYN Observatory is a joint facility of the University of Wisconsin–Madison, Indiana University, the National Optical Astronomy Observatory and the University of Missouri.

over six nights: 2014 January 20–23, 2014 February 12, 2014 February 13, 2014 February 15. These spectroscopic data were taken in conjunction with the data used in our previously published abundance study of the GC NGC 5053 (Boberg et al. 2015), and therefore used the same general setup of the Hydra multi-object spectrograph and Bench Spectrograph. As with our study of NGC 5053, the resulting spectra cover a wavelength range of approximately 6063–6380 Å with typical signal-to-noise ratios (S/Ns) of 80–120, and a dispersion of 0.16 Å pixel^{−1} ($R \approx 18,000$). In addition to our science targets a number of radial velocity standards and a hot, rapidly rotating, B star were observed at the beginning of each night. These calibration targets were observed in order to measure the radial velocities of our science targets and remove telluric features from their spectra.

The data reductions were performed using IRAF³ following the outline given in Boberg et al. (2015). As an additional step, the spectra in this study were cleaned of cosmic rays using the spectroscopic version of LA-Cosmic (van Dokkum 2001). In total, each program star was observed for 4.5 hr divided into six 2400 s exposures. The final reduced and cleaned individual spectra were combined using the IRAF task *scombine*.

2.2. Target Selection

Our science targets were taken from stars in the photometry published by Rey et al. (1998) with V magnitudes less than 15.5. The stars from Rey et al. (1998) that met this magnitude cut are shown in a V versus ($B - V$) CMD in the left-hand panel of Figure 1. In order to remove possible photometric interlopers from our sample, we used the radial velocities (RV) of each star as measured by the *fxcor* task in the NOAO package in IRAF.

Each star was cross-correlated against 2–3 radial velocity standards observed on the same night. The mean standard deviation of the individual measurements for a given star was 0.1 km s^{−1} and the average error on the measurements was 1.1 km s^{−1}, as estimated by *fxcor*. The RV for each star is given in Table 2. The listed RV values are the average of the individual measurements made by using the different standards. The uncertainty listed with this value is the mean of the measurement errors as given by *fxcor* for each standard star. The average standard deviation of the radial velocity measurements for the 27 stars observed on multiple nights is 0.41 km s^{−1}. The final column in Table 2 gives a membership flag for each star in the sample. Cluster members and non-members are designated by Y and N flags, respectively. Stars listed in Table 2 with bold N flags are stars that have radial

³ IRAF is distributed by the National Optical Astronomy Observatories, which are operated by the Association of Universities for Research in Astronomy, Inc., under cooperative agreement with the National Science Foundation.

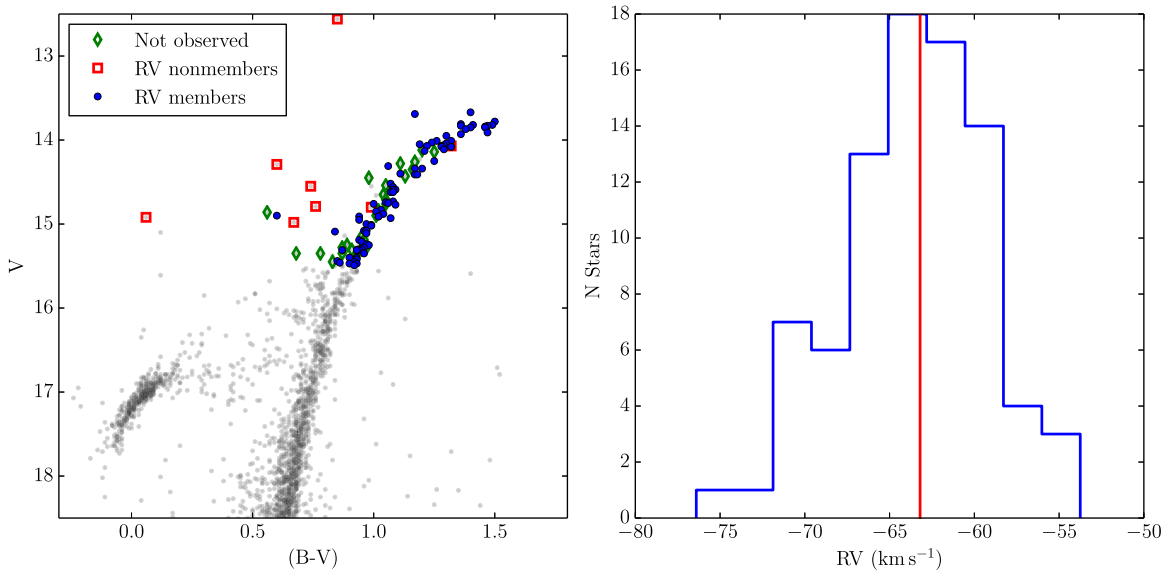


Figure 1. Left: V vs. $(B - V)$ CMD for M53. Data taken from Rey et al. (1998). The points overplotted with open squares and filled circles are stars for which we collected spectra. The filled circles mark stars that are considered to be cluster members based on their photometry and radial velocities. The squares mark the stars that were bright enough to observe but had radial velocities inconsistent with cluster membership. The diamonds mark the stars that met the V magnitude criterion, but were not observed during our run. Right: histogram of radial velocities for stars we are considering as cluster members. The non-members are not included in this histogram because they are too far removed (3σ) from the cluster mean and would skew the x -axis of the plot. The vertical line marks the radial velocity of the cluster as found by Kimmig et al. (2015).

velocities consistent with the systemic cluster velocity, but the spectral analysis did not converge on a solution for the atmospheric parameters for these stars. We consider these stars to be non-members and possibly photometric interlopers. The average radial velocity of our stars designated as cluster members is $-63.2 \pm 0.5 \text{ km s}^{-1}$. This systemic cluster velocity is in agreement with the previously determined value $RV = -62.8 \pm 0.3 \text{ km s}^{-1}$ from Kimmig et al. (2015). The radial velocity distribution of the stars in our sample is shown in the right-hand panel of Figure 1. The non-members are not included in this plot because they sit more than 3σ from the cluster peak. In Figure 2 we plot our targets on a DSS image centered on the cluster. The markers are color coded according to their radial velocity.

3. ANALYSIS

3.1. Atmospheric Parameters

As a starting point for the effective temperature (T_{eff}) and the bolometric correction in V (BC_V), we applied the relationships from Alonso et al. (1999) using the $(B - V)$, $(V - K)$, and $(J - K)$ colors. The J , H , and K magnitudes were taken from 2MASS (Skrutskie et al. 2006). The colors were dereddened with an $E(B - V) = 0.02$ (Harris 1996, 2010 Version), following the relations found by Rieke & Lebofsky (1985). Surface gravities were calculated based on the derived effective temperatures and bolometric corrections assuming a mass of $0.8M_{\odot}$ for every star in the sample and a distance modulus of $(m - M)_V = 16.32$ (Harris 1996, 2010 Version). For many of the stars, there were enough Fe I lines to adjust the T_{eff} to remove trends in Fe I abundance with excitation potential. In these cases, the T_{eff} was not changed by more than 100 K. There were not, however, enough Fe II lines available in our spectral window to use the ionization equilibrium to adjust the surface gravities so they were kept at their photometrically estimated values.

Following the procedure in Boberg et al. (2015) initial estimates of microturbulent velocities (v_t) were based on the average of the relationships found in three different studies (Pilachowski et al. 1996; Carretta et al. 2004; Johnson et al. 2008). These first estimates were adjusted through the course of the Fe I abundance analysis to remove the dependence of derived $[\text{Fe}/\text{H}]$ abundance on Fe I line strength. MARCS LTE model atmospheres (Gustafsson et al. 2008) were interpolated to the photometrically and spectroscopically determined atmospheric parameters in order to be used in the abundance analysis. Our final values for the atmospheric parameters are given in Table 3.

3.2. EW Measurements

We measured the EW of Fe I, Ni I, Ti I, and Ca I lines in the M53 spectra to determine the abundances of each of the listed species. This is the same set of species that we measured in Boberg et al. (2015). The EW measurements of the Fe I lines were made in a semi-automated way with the ARESv2 program (Sousa et al. 2015). If the error on the ARES EW measurement of a given Fe I line was $>10 \text{ m\AA}$, and/or the line was slightly blended, the line was measured by hand. The spectra were also checked for lines that were missed by the ARES program and they were measured by hand if they were indeed present and good lines. To detect the presence of blends and confirm the location of lines, we compared our spectra to the solar spectrum from Wallace et al. (2011). All of the Ni I, Ti I, and Ca I lines were measured by hand using the *splot* task in IRAF. To be consistent with our previous study, we used the same line list from the *Gaia*-ESO Survey (Heiter et al. 2015). The EW measurements and atomic parameters for all lines will be available through an online table. We provide a sample of this table in Table 4. The abundances were determined using the *abfind* task in the 2010 August version of MOOG (Snedden 1973) with the solar abundances as found by Anders & Grevesse (1989).

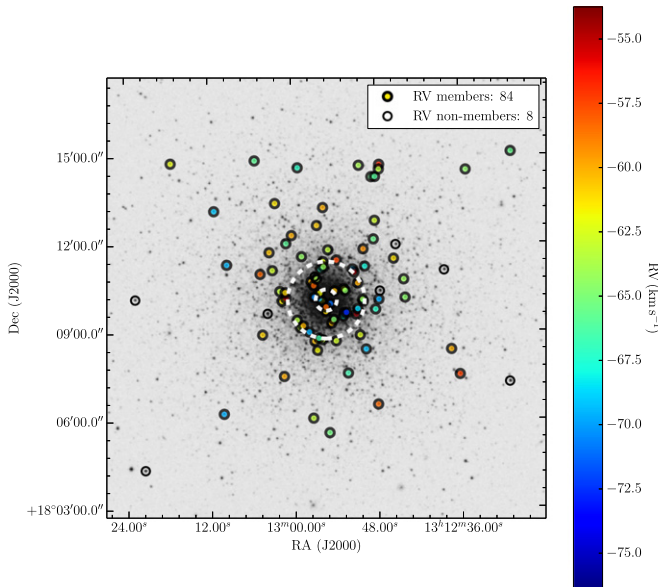
Table 2
Observational Data

ID	R.A.	Decl.	V	M_V	$(B - V)_0$	$(V - K)_0$	RV	σ_{RV}	S/N	n obs.	Member
Rey et al.	J2000	J2000					(km s ⁻¹)	(km s ⁻¹)			Y/N
1	13:12:56.88	+18:10:53.20	12.56	-3.76	0.83	1.891	-22.2	1.4	77	1	N
2	13:12:55.32	+18:09:42.04	13.67	-2.65	1.38	3.195	-60.9	1.1	72	1	Y
3	13:12:55.85	+18:10:03.88	13.69	-2.63	1.15	2.845	-62.1	1.0	110	1	Y
4	13:12:45.53	+18:11:28.96	13.78	-2.54	1.48	3.285	-61.3	1.0	138	2	Y
5	13:12:56.23	+18:10:08.28	13.81	-2.51	1.34	3.215	-69.9	0.8	139	1	Y
6	13:12:51.41	+18:11:08.02	13.82	-2.50	1.47	0.175	-69.7	2.1	83	2	N
7	13:12:57.72	+18:09:00.60	13.82	-2.50	1.39	3.135	-69.7	1.5	94	1	Y
8	13:12:28.58	+18:15:05.12	13.83	-2.49	1.45	3.195	-65.7	1.2	137	3	N
9	13:13:01.58	+18:10:03.91	13.83	-2.49	1.34	3.105	-61.5	1.1	115	1	Y
10	13:12:55.66	+18:11:23.71	13.84	-2.48	1.44	3.275	-62.3	0.7	107	1	Y
11	13:12:56.16	+18:10:19.45	13.85	-2.47	1.38	3.145	-61.8	0.7	115	1	Y
12	13:12:56.57	+18:08:23.13	13.85	-2.47	1.44	3.275	-61.7	0.8	120	1	Y
13	13:12:54.50	+18:09:18.13	13.87	-2.45	1.36	3.195	-60.4	0.8	133	1	Y
14	13:13:04.68	+18:10:59.46	13.91	-2.41	1.45	3.145	-58.3	1.2	74	2	Y
15	13:12:50.95	+18:09:36.08	13.93	-2.39	1.34	3.155	-53.8	1.9	66	1	Y
16	13:12:59.16	+18:14:35.60	13.95	-2.37	1.28	2.945	-66.7	1.4	104	5	N
17	13:12:56.93	+18:10:11.46	14.01	-2.31	1.24	2.985	-70.5	1.2	72	1	Y
18	13:12:50.69	+18:10:39.63	14.01	-2.31	1.30	3.045	-59.9	0.8	115	1	Y
19	13:12:54.65	+18:09:58.05	14.03	-2.29	1.22	3.055	-71.1	1.0	134	1	Y
20	13:12:56.95	+18:08:41.91	14.04	-2.28	1.28	3.015	-60.4	0.9	131	1	Y
21	13:12:54.19	+18:09:25.79	14.05	-2.27	1.17	3.075	-64.9	0.9	135	1	Y
22	13:12:54.05	+18:10:23.78	14.06	-2.26	1.27	2.955	-60.5	1.6	58	1	Y
23	13:13:03.67	+18:09:38.80	14.07	-2.25	1.30	3.017	370.1	55.9	51	1	N
24	13:12:52.80	+18:09:32.37	14.07	-2.25	1.26	2.985	-67.9	0.8	127	1	Y
25	13:12:55.27	+18:09:51.24	14.07	-2.25	1.20	2.945	-58.5	0.9	134	1	Y
26	13:13:01.03	+18:10:09.51	14.08	-2.24	1.30	2.775	-54.4	1.6	56	1	Y
27	13:12:37.37	+18:08:23.21	14.08	-2.24	1.30	3.085	60.1	0.9	138	2	Y
28	13:12:52.73	+18:10:28.01	14.08	-2.24	1.26	2.965	-62.2	1.0	128	1	Y
29	13:12:50.42	+18:08:53.66	14.11	-2.21	1.27	3.055	-62.4	0.9	137	2	Y
31	13:12:57.38	+18:10:43.30	14.13	-2.19	1.19	2.855	-60.4	1.1	67	1	Y
34	13:12:55.82	+18:08:44.80	14.25	-2.07	1.23	2.885	-63.2	0.7	124	1	Y
37	13:12:29.05	+18:07:16.10	14.29	-2.03	0.580	1.436	0.5	1.0	49	1	N
38	13:13:02.93	+18:11:06.66	14.31	-2.01	1.04	2.755	-62.8	1.0	77	1	Y
39	13:12:47.69	+18:10:06.09	14.34	-1.98	1.15	2.815	-69.7	1.1	86	1	Y
40	13:12:48.60	+18:14:15.71	14.34	-1.98	1.18	2.915	-65.7	1.4	132	2	Y
42	13:12:54.94	+18:11:47.65	14.40	-1.92	1.09	2.675	-63.2	1.2	123	1	N
43	13:12:56.35	+18:08:47.90	14.41	-1.91	1.15	2.785	-66.5	1.0	129	1	Y
44	13:12:43.94	+18:10:09.27	14.41	-1.91	1.16	2.845	-64.7	0.9	126	2	Y
47	13:12:56.02	+18:11:08.29	14.52	-1.80	1.05	2.755	-67.0	0.9	92	1	Y
49	13:12:47.54	+18:10:23.20	14.55	-1.77	0.72	1.610	9.2	1.0	92	1	N
51	13:13:17.35	+18:14:46.36	14.56	-1.76	1.06	2.625	-62.1	1.2	131	4	Y
52	13:12:57.02	+18:10:35.06	14.59	-1.73	1.07	2.685	-58.2	1.2	52	1	Y
53	13:12:48.19	+18:12:46.60	14.59	-1.73	1.06	2.725	-62.8	1.1	119	5	Y
54	13:13:05.30	+18:14:50.88	14.62	-1.70	1.05	2.625	-65.8	1.1	99	4	Y
55	13:12:49.90	+18:10:02.40	14.62	-1.70	1.06	2.675	-67.0	1.0	100	1	Y
60	13:12:57.26	+18:06:05.01	14.73	-1.59	1.06	2.605	-62.2	1.3	123	3	Y
61	13:12:55.58	+18:13:13.88	14.74	-1.58	1.03	2.575	-60.1	1.0	116	4	Y
62	13:12:52.70	+18:09:39.28	14.75	-1.57	1.04	2.675	-76.4	1.2	119	1	Y
64	13:13:00.94	+18:12:01.22	14.76	-1.56	0.98	2.705	-66.0	2.3	57	1	Y
65	13:12:36.17	+18:07:32.00	14.77	-1.55	1.07	2.655	-57.2	1.0	109	5	Y
66	13:13:21.44	+18:04:21.40	14.79	-1.53	0.74	1.765	-39.5	1.1	76	1	N
67	13:12:38.30	+18:11:04.70	14.80	-1.52	0.92	2.445	-68.7	1.4	103	1	N
68	13:13:02.47	+18:13:23.40	14.83	-1.49	1.01	2.585	-61.1	0.9	118	3	Y
70	13:12:48.10	+18:14:15.97	14.85	-1.47	0.99	2.595	-66.1	1.1	108	2	Y
72	13:12:47.95	+18:06:32.06	14.88	-1.44	1.02	2.595	-58.4	1.2	90	3	Y
75	13:13:11.21	+18:13:08.36	14.90	-1.42	0.58	1.495	-69.1	1.2	73	3	Y
76	13:12:50.74	+18:09:47.27	14.91	-1.41	0.92	2.445	-68.7	1.4	103	1	N
77	13:13:03.36	+18:11:43.40	14.91	-1.41	1.00	2.705	-60.6	1.9	65	1	Y
78	13:12:55.61	+18:11:13.03	14.91	-1.41	1.00	2.535	-64.3	1.4	92	1	Y
79	13:12:45.21	+18:11:57.50	14.92	-1.40	0.04	0.569	N
80	13:12:52.37	+18:09:40.03	14.93	-1.39	1.05	2.655	-72.5	1.1	101	1	Y
81	13:13:01.90	+18:10:23.84	14.95	-1.37	0.92	2.435	-63.2	1.1	87	1	N
82	13:13:22.64	+18:10:09.40	14.98	-1.34	0.65	1.468	-12.6	1.1	49	1	N

Table 2
(Continued)

ID	R.A.	Decl.	V	M_V	$(B - V)_0$	$(V - K)_0$	RV	σ_{RV}	S/N	n obs.	Member
Rey et al.	J2000	J2000					(km s ⁻¹)	(km s ⁻¹)			Y/N
83	13:12:59.45	+18:09:25.10	15.00	-1.32	0.95	2.485	-63.5	1.3	96	1	N
84	13:13:09.46	+18:11:18.86	15.01	-1.31	0.97	2.515	-69.5	1.3	68	1	Y
85	13:12:58.99	+18:09:09.73	15.02	-1.30	0.97	2.505	-63.2	0.9	85	1	Y
86	13:12:54.96	+18:05:35.10	15.08	-1.24	0.94	2.405	-65.4	1.5	113	5	Y
87	13:12:49.87	+18:11:48.76	15.08	-1.24	0.95	2.545	-59.3	1.0	85	1	Y
88	13:12:52.51	+18:10:24.49	15.08	-1.24	0.95	2.575	-64.5	1.1	113	1	Y
89	13:12:56.59	+18:10:48.30	15.09	-1.23	0.82	2.135	-63.8	3.1	48	1	Y
91	13:12:49.68	+18:11:13.57	15.11	-1.21	0.95	2.835	-67.8	1.3	98	1	Y
95	13:12:58.56	+18:09:13.50	15.19	-1.13	0.92	2.455	-60.1	1.3	89	1	Y
97	13:12:56.50	+18:12:37.52	15.21	-1.11	0.93	2.505	-60.3	1.5	115	1	Y
99	13:13:04.42	+18:08:55.64	15.24	-1.08	0.95	2.505	-60.8	1.4	58	2	Y
101	13:12:35.06	+18:14:28.68	15.25	-1.07	0.96	2.525	-64.6	1.0	101	3	Y
104	13:12:53.88	+18:08:41.99	15.28	-1.04	0.94	2.485	-62.6	1.1	105	1	Y
107	13:13:00.12	+18:12:17.66	15.30	-1.02	0.92	2.445	-60.1	1.1	98	3	Y
108	13:12:44.09	+18:10:46.57	15.30	-1.02	0.93	2.495	-64.2	1.1	93	1	Y
110	13:12:50.04	+18:10:06.12	15.31	-1.01	0.92	2.475	-64.2	1.1	107	1	Y
111	13:12:50.38	+18:14:39.15	15.31	-1.01	0.91	2.485	-63.8	1.2	70	4	Y
112	13:12:49.61	+18:08:24.67	15.31	-1.01	0.85	2.315	-69.2	1.4	96	1	Y
113	13:13:01.13	+18:10:21.35	15.31	-1.01	0.91	2.465	-60.9	1.5	69	1	Y
118	13:12:58.70	+18:11:34.41	15.35	-0.97	0.94	2.395	-64.4	1.2	99	1	Y
122	13:12:48.38	+18:12:08.72	15.40	-0.92	0.88	2.425	-65.5	1.4	68	1	Y
123	13:12:51.22	+18:11:02.02	15.40	-0.92	0.91	4.125	-54.0	1.1	76	1	N
124	13:12:47.47	+18:14:40.57	15.42	-0.90	0.91	2.475	-56.7	1.0	89	1	Y
126	13:12:48.17	+18:09:45.87	15.44	-0.88	0.83	3.015	-67.3	1.4	111	1	N
128	13:13:10.08	+18:06:15.20	15.45	-0.87	0.90	2.435	-69.8	1.4	93	5	Y
129	13:13:01.39	+18:07:30.72	15.46	-0.86	0.84	2.315	-59.9	1.4	89	3	Y
130	13:12:52.20	+18:07:36.14	15.47	-0.85	0.88	2.335	-66.6	1.0	81	1	Y
131	13:12:47.52	+18:14:31.05	15.47	-0.85	0.91	2.435	-63.5	1.2	86	1	Y
132	13:12:53.74	+18:11:26.65	15.49	-0.83	0.90	2.375	-57.5	1.1	72	1	Y

(This table is available in machine-readable form.)

**Figure 2.** A $15' \times 15'$ DSS image centered on M53. The RV members are marked with colored circles according to their individual radial velocities. The radial velocity non-members are marked with open black circles. The number of stars in each sample is given in the legend. The core and half light radii are shown as dashed white circles, respectively. The values for these radii were taken from the 2010 version of Harris (1996).

3.3. Spectral Synthesis

To measure the Na, O, and Ba abundances in M53 we used the *synth* task in MOOG. For the Na and O abundances spectral synthesis is required to account for the presence of blends and molecular bands, and in the case of Ba, to account for hyperfine structure and the isotopic mix of the species. The final abundance of each of these species was determined by generating synthetic spectra with the atmospheric parameters determined through the EW analysis of the Fe I lines. The Gaussian broadening of the synthetic spectra was determined by matching the FWHM of lines of other species in the spectra that were clean and free of blends or other features. The Na, O, and Ba abundances in these synthetic spectra were adjusted to match the spectral feature being measured to arrive at the final abundance of the species. This final value was then slightly adjusted to determine how precisely we could measure the Na, O, and Ba abundances. Examples of the spectral synthesis are shown in Figure 3.

This study used the same Na, O and Ba lines as our previous study to determine their respective abundances. The Na abundance is measured from the Na I lines at 6154 Å and 6160 Å, the O abundance is measured from the [O I] line at 6300 Å, and the Ba abundance is measured from the Ba II line at 6141 Å. As we note in Boberg et al. (2015) the Na I line at 6154 Å is often too weak to measure, so the [Na/Fe]

Table 3
Derived Atmospheric Parameters

ID	T_{eff} (K)	BC_v	$\log(g)$ (cm s^{-2})	v_t (km s^{-1})
3	4380	-0.56	0.7	1.60
4	4050	-0.80	0.5	2.25
5	4130	-0.72	0.6	1.88
7	4140	-0.74	0.5	2.02
9	4180	-0.70	0.6	1.96
10	3965	-0.79	0.5	1.88
11	4170	-0.71	0.6	1.91
13	4050	-0.69	0.6	1.87
14	4050	-0.72	0.6	1.98
18	4225	-0.66	0.7	1.95
19	4280	-0.63	0.7	1.65
20	4260	-0.66	0.7	1.98
21	4270	-0.74	0.6	1.75
24	4215	-0.68	0.7	1.88
25	4250	-0.64	0.6	1.60
27	4200	-0.71	0.7	1.92
28	4260	-0.66	0.7	1.75
29	4200	-0.69	0.6	1.69
34	4310	-0.61	0.8	1.83
39	4460	-0.57	0.9	1.92
40	4275	-0.61	0.9	1.88
43	4375	-0.58	0.9	1.72
44	4375	-0.60	1.0	1.94
47	4480	-0.53	1.0	1.87
51	4450	-0.50	1.1	1.90
53	4440	-0.53	1.1	1.85
54	4460	-0.49	1.1	1.75
55	4450	-0.52	1.1	1.82
60	4500	-0.50	1.1	2.00
61	4500	-0.51	1.1	1.60
62	4500	-0.49	1.2	1.61
65	4425	-0.53	1.1	1.73
68	4500	-0.48	1.2	1.80
70	4450	-0.47	0.6	1.58
72	4540	-0.49	1.2	1.90
78	4525	-0.49	1.2	1.55
80	4440	-0.53	1.2	1.63
85	4650	-0.45	1.3	1.87
86	4670	-0.42	1.4	1.98
87	4580	-0.45	1.3	1.70
88	4540	-0.47	1.3	1.76
91	4575	-0.49	1.3	1.60
95	4660	-0.42	1.4	1.52
97	4575	-0.46	1.4	1.56
101	4525	-0.46	1.4	1.76
104	4525	-0.46	1.4	1.56
108	4570	-0.45	1.4	1.80
110	4525	-0.42	1.5	1.87
112	4820	-0.36	1.4	1.75
118	4600	-0.42	1.5	1.68
128	4675	-0.43	1.5	1.80
129	4775	-0.38	1.6	1.64
131	4650	-0.41	1.5	1.95
132	4550	-0.40	1.6	1.70

Table 4
Equivalent Widths

Element	λ (Å)	$\log(gf)$	EP (eV)	EW (mÅ)
Ca I	6122.217	-0.316	1.886	138.9
Ca I	6169.563	-0.478	2.526	67.2
Ca I	6102.723	-0.793	1.879	999.9
Ca I	6166.439	-1.142	2.521	999.9
Ca I	6169.042	-0.797	2.523	57.0

(This table is available in its entirety in machine-readable form.)

by the fact that it is both an *s*- and *r*-process neutron capture element. Following our previous analysis in NGC 5053, and the findings of McWilliam (1998), we assume that the Ba in M53 is only the result of the *r*-process, and therefore only contains the following isotopes: ^{135}Ba , ^{137}Ba , ^{138}Ba , with a ratio of of 40:32:28, respectively. For a full discussion about the basis of these assumptions see McWilliam (1998).

3.4. Uncertainties

We followed the same procedure as in our study of NGC 5053 to determine the sensitivity of our abundance measurements to variations in the atmospheric parameters. In this procedure the abundances of each species are remeasured with one of the atmospheric parameters varied (e.g., T_{eff}), while the others are held constant. This process was repeated until each of the atmospheric parameters used in measuring the abundances was varied over a large enough range of values to quantify how their individual uncertainties contribute to the errors in the abundance measurements. This procedure was performed on a star with the following atmospheric parameters over the range indicated with each value: $T_{\text{eff}} = 4310 \pm 100$ (K), $\log g = 0.8 \pm 0.2$ (cgs), $[\text{M}/\text{H}] = -2.01 \pm 0.2$ (dex), $v_t = 1.83 \pm 0.25$ km s^{-1} .

The results of this procedure are given in Table 5, where each abundance is listed with a $\sigma_{\text{obs.}}$ and σ_{total} value. For abundances determined using EWs, $\sigma_{\text{obs.}}$ is the standard deviation of abundances determined from the number of lines listed in the table for a single star. In cases where only one line was measured this field is left blank. For those abundances that were determined with spectral synthesis (Na, O, Ba), $\sigma_{\text{obs.}}$ is the error assigned to each abundance as described in the previous section. To calculate σ_{total} , we added the uncertainties from the atmospheric parameters in quadrature. From this analysis we see that our observed uncertainty is consistent with that expected from variations in atmospheric parameters.

4. RESULTS

4.1. Fe, Ca, Ti, Ni, Ba

We present the final Fe, Ca, Ti, Ni, and Ba abundances for the stars in our sample in Table 6. Those stars that were determined to not be cluster members, or where we were unable to measure the abundances, are not listed in this table. Each star is listed with the number of lines measured in determining the final values given, as well as the standard deviation of these measurements as reported by MOOG. The assumed solar values used in calculating our final abundance ratios are listed in the final row of Table 6. In Figure 4 we plot the $[\text{Fe}/\text{H}]$ abundance of each star versus its respective T_{eff} , V

abundances are for the most part determined by the line at 6160 Å. Additionally, the [O I] line is in a spectral region with a large amount of telluric contamination. These features were removed before determining [O/Fe] abundances by using the IRAF task *telluric* with the spectrum of a hot B star used as the telluric template. Determining the Ba abundance is complicated

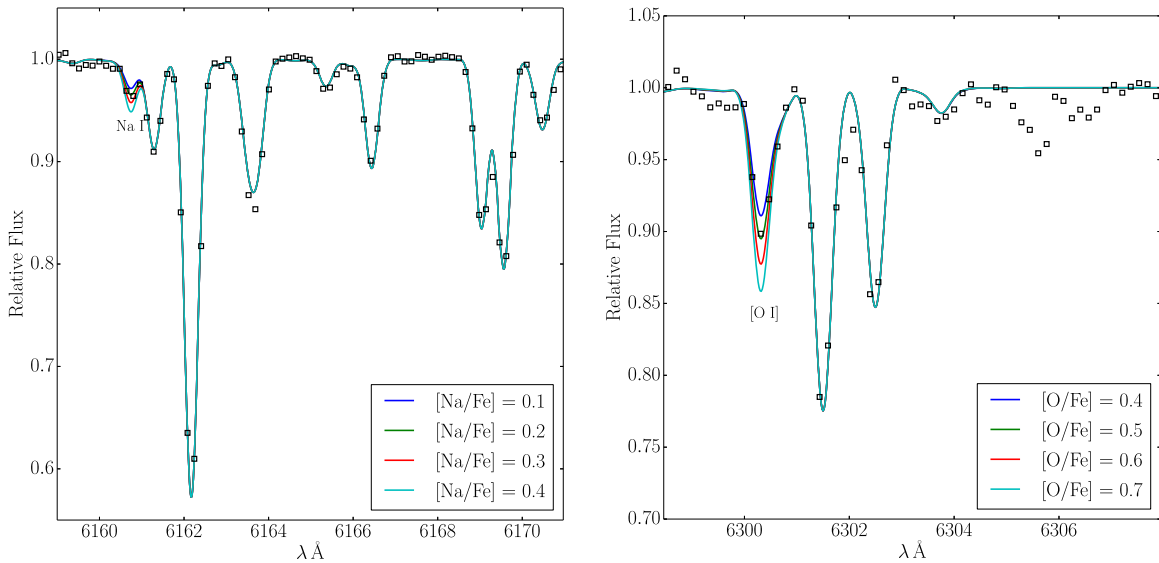


Figure 3. An example of the spectral synthesis performed to determine the Na and O abundances for Star 27. Left panel: the spectral region around the Na I line near 6160 Å. The strong line located at approximately 6162 Å is a Ca I line. Right panel: the spectral window near the [O I] line near 6300 Å. In each panel the data are plotted as black squares. The spectrum in the right-hand panel has been corrected for telluric features.

Table 5
Uncertainties on Atmospheric Parameters

Ion	$T_{\text{eff}} \pm 100(\text{K})$ (dex)	$\log g \pm 0.20(\text{cgs})$ (dex)	$[\text{M}/\text{H}] \pm 0.10(\text{dex})$ (dex)	$v_t \pm 0.25(\text{km s}^{-1})$ (dex)	σ_{total} (dex)	No. Lines	σ_{obs} (dex)
Fe I	± 0.18	± 0.03	± 0.02	∓ 0.06	0.19	27	0.11
[O I]	± 0.05	± 0.10	± 0.05	± 0.00	0.12	1	0.10
Na I	± 0.10	± 0.03	± 0.05	∓ 0.00	0.12	1	0.10
Ca I	± 0.11	± 0.01	± 0.04	∓ 0.06	0.13	3	0.07
Ti I	± 0.20	± 0.02	± 0.03	∓ 0.05	0.21	4	0.25
Ni I	± 0.13	± 0.03	± 0.01	∓ 0.09	0.17	2	0.04
Ba II	± 0.08	± 0.08	± 0.05	∓ 0.05	0.11	1	0.10

magnitude, $\log(g)$, and v_t . The error bars on the plot represent the standard deviation of the $[\text{Fe}/\text{H}]$ measurement as reported by MOOG. The solid line shown in each panel marks the location of the mean $[\text{Fe}/\text{H}]$ abundance of the sample. The two red dashed lines mark the mean $[\text{Fe}/\text{H}]$ of the sample $\pm 1\sigma_{[\text{Fe}/\text{H}]}$. From these relationships we find that there are no statistically significant trends in $[\text{Fe}/\text{H}]$ with any of the atmospheric parameters plotted. The distributions of Ca, Ni, Ti, and Ba abundances are illustrated as a box-and-whisker plot in the left-hand panel of Figure 5. The numbers given below the boxes in this plot are the median abundance values of each species, as well as their respective standard deviations in our sample. The right-hand panel of this plot will be explained in the discussion section.

4.2. Na and O

We were able to measure the $[\text{Na}/\text{Fe}]$ and $[\text{O}/\text{Fe}]$ abundances in 46 of the 53 cluster members in our sample using spectral synthesis. There were 3 stars for which we were able to measure the $[\text{Na}/\text{Fe}]$ abundance and not $[\text{O}/\text{Fe}]$. In these cases the sky subtraction left large enough residuals to cause the [O I] line to be unmeasurable. In the 4 stars without $[\text{Na}/\text{Fe}]$ or $[\text{O}/\text{Fe}]$ the spectra were too noisy to determine either of the abundances. These abundances are listed in Table 7. Following the models provided by Lind et al. (2011), the largest NLTE correction that would have to be applied to

$[\text{Na}/\text{Fe}]$ in our stars is -0.05 dex, which is a factor of 2 less than the precision with which we are able to measure the Na abundance with our data. The typical NLTE corrections were even smaller at -0.01 dex. The $[\text{Na}/\text{Fe}]$ abundances listed in Table 7, and plotted in Figure 6, have not been corrected for NLTE effects. Those $[\text{Na}/\text{Fe}]$ abundances listed with ($<$) for their errors are upper limits. In Figure 6 we plot the $[\text{Na}/\text{Fe}]$ abundances versus $[\text{O}/\text{Fe}]$ along with their histograms. The details of Figure 6 will be explained in the discussion section.

4.3. Comparison with Literature

Two studies have recently measured abundances for a small sample of RGB stars in M53. Lamb et al. (2015) collected optical and infrared spectra for two RGB stars in M53, and Mészáros et al. (2015) analyzed the spectra of 16 RGB cluster members that were collected as part of the APOGEE survey. The infrared data used by Lamb et al. (2015) were the same APOGEE data used by Mészáros et al. (2015). Both of the stars in Lamb et al. (2015) sample and 15 of the 16 stars in Mészáros et al. (2015) were observed as part of this study. The two M53 stars in Lamb et al. (2015) are also found in Mészáros et al. (2015). A comparison of the two stars in common between these two studies, as well as ours, is given in Table 8. The abundances from Lamb et al. (2015) are those determined from their optical spectra. The stars from the Mészáros et al. (2015) study are listed with their 2MASSID as presented in that paper.

Table 6
Fe, Ca, Ti, Ni, and Ba Abundances in M53

ID	[Fe/H]	σ_{Fe}	n	[Ca/Fe]	σ_{Ca}	n	[Ti/Fe]	σ_{Ti}	n	[Ni/Fe]	σ_{Ni}	n	[Ba/Fe]	σ_{Ba}	n
3	-2.10	0.08	15	0.44	0.09	4	0.26	0.06	2	-0.01	0.10	2	0.10	0.1	1
4	-2.22	0.07	21	0.36	0.06	5	0.25	0.18	4	-0.02	0.06	2	0.10	0.1	1
5	-2.26	0.08	21	0.33	0.08	6	0.20	0.09	3	-0.04	0.08	3	0.10	0.1	1
7	-2.03	0.04	14	0.32	0.10	3	0.06	0.09	3	0.09	0.00	1	0.10	0.1	1
9	-2.02	0.08	15	0.36	0.08	3	0.15	0.08	3	-0.06	0.09	2	0.10	0.1	1
10	-2.07	0.12	22	0.10	0.06	5	-0.13	0.05	3	-0.08	0.14	3	0.15	0.1	1
11	-2.04	0.12	29	0.34	0.04	6	0.26	0.16	5	-0.08	0.08	2	0.30	0.1	1
13	-2.17	0.07	20	0.26	0.05	5	-0.01	0.03	3	-0.01	0.04	3	0.30	0.1	1
14	-2.03	0.04	17	0.08	0.07	5	-0.10	0.06	3	-0.01	0.07	3	0.20	0.1	1
18	-2.10	0.06	19	0.32	0.07	6	0.18	0.03	3	0.04	0.00	1	0.40	0.1	1
19	-1.95	0.11	33	0.35	0.07	4	0.09	0.05	4	-0.10	0.06	2	0.20	0.1	1
20	-2.13	0.10	15	0.33	0.08	6	0.20	0.17	3	-0.13	0.16	2	0.10	0.1	1
24	-2.21	0.13	24	0.42	0.04	4	0.18	0.02	4	0.00	0.10	3	0.10	0.1	1
25	-2.05	0.12	28	0.36	0.17	4	0.23	0.18	4	-0.16	0.04	2	0.20	0.1	1
27	-2.11	0.12	32	0.36	0.05	6	0.13	0.05	3	-0.03	0.03	4	0.20	0.1	1
28	-2.06	0.11	23	0.36	0.06	5	0.11	0.07	3	-0.05	0.06	2	0.15	0.1	1
29	-1.96	0.11	28	0.31	0.07	4	0.13	0.01	2	-0.11	0.03	3	0.30	0.1	1
34	-2.01	0.11	27	0.39	0.07	3	0.30	0.25	4	-0.12	0.04	2	0.40	0.1	1
39	-1.88	0.10	7	0.29	0.12	3	-0.10	...	1	0.16	0.00	1	0.10	0.1	1
40	-2.13	0.10	27	0.35	0.06	4	0.16	0.14	3	-0.02	0.13	3	0.30	0.1	1
43	-2.02	0.14	30	0.34	0.06	6	0.16	0.11	4	-0.13	0.28	2	0.20	0.1	1
44	-2.03	0.14	16	0.35	0.15	7	0.20	0.06	3	-0.04	0.13	4	0.20	0.1	1
47	-2.09	0.13	16	0.39	0.11	3	0.31	0.07	3	0.05	0.16	2	0.20	0.1	1
51	-2.10	0.19	28	0.32	0.15	8	0.16	0.42	4	-0.08	0.19	2	0.25	0.1	1
53	-2.13	0.10	13	0.33	0.10	6	0.19	0.08	2	-0.26	0.11	2	0.30	0.1	1
54	-2.14	0.14	18	0.38	0.14	4	0.14	0.08	3	-0.22	0.12	2	0.10	0.1	1
55	-2.09	0.10	17	0.41	0.12	3	0.17	0.03	2	0.09	0.03	2	0.10	0.1	1
60	-2.09	0.08	23	0.34	0.07	5	0.41	0.36	4	-0.01	0.11	2	0.00	0.1	1
61	-2.00	0.11	26	0.41	0.09	6	0.17	0.13	2	-0.16	0.33	2	0.10	0.1	1
62	-2.09	0.10	23	0.33	0.15	6	0.25	0.11	2	0.00	0.14	3	0.30	0.1	1
65	-2.07	0.09	25	0.39	0.09	6	0.30	0.10	3	0.02	0.21	3	0.10	0.1	1
68	-2.12	0.09	24	0.39	0.06	6	0.20	0.13	2	0.02	0.13	2	0.10	0.1	1
70	-2.04	0.14	25	0.38	0.04	4	0.24	0.48	3	-0.14	0.14	2	0.40	0.1	1
72	-2.05	0.16	15	0.34	0.12	4	0.27	...	1	-0.27	0.00	1	0.10	0.1	1
78	-2.11	0.15	17	0.40	0.14	3	0.31	...	1	0.22	0.00	1	0.10	0.1	1
80	-2.06	0.11	16	0.42	0.06	3	0.29	0.23	2	-0.23	0.00	1	0.40	0.1	1
85	-1.91	0.11	12	0.39	0.14	2	0.26	0.15	2	-0.06	0.29	3	0.00	0.1	1
86	-2.13	0.11	18	0.39	0.10	6	1	-0.21	0.00	1	0.30	0.1	1
87	-2.16	0.10	15	0.45	0.01	2	0.04	0.17	2	-0.25	0.00	1	0.10	0.1	1
88	-2.07	0.11	22	0.41	0.07	3	0.20	0.04	2	0.02	0.06	2	0.10	0.1	1
91	-2.05	0.13	13	0.44	0.08	3	0.16	...	1	0.09	0.27	2	0.10	0.1	1
95	-2.12	0.14	8	0.53	0.20	2	0.59	...	1	0.16	0.66	4	0.20	0.1	1
97	-2.11	0.11	13	0.54	0.02	2	0.21	0.02	2	-0.39	0.00	1	0.20	0.1	1
101	-1.90	0.08	16	0.36	0.05	3	0.21	0.01	2	0.13	0.00	1	0.15	0.1	1
104	-2.07	0.15	22	0.33	0.12	7	0.21	0.17	3	-0.03	0.38	2	0.20	0.1	1
108	-2.14	0.09	15	0.34	0.10	5	0.19	...	1	-0.02	0.00	1	0.10	0.1	1
110	-2.10	0.12	23	0.36	0.04	4	0.05	0.04	2	-0.08	0.16	3	0.10	0.1	1
112	-2.03	0.08	11	0.39	0.01	2	0	-0.09	0.00	1	0.10	0.1	1
118	-2.01	0.09	16	0.46	0.06	2	0	-0.02	0.25	2	0.00	0.1	1
128	-2.08	0.11	14	0.26	0.13	3	0.33	0.28	3	0.16	0.00	1	0.00	0.1	1
129	-2.00	0.11	18	0.55	0.18	2	0	0	0.70	0.1	1
131	-2.06	0.14	15	0.27	0.14	2	0.30	...	1	0.010	0.25	2	0.00	0.1	1
132	-2.15	0.08	10	0.47	0.11	3	0.22	...	1	0	0.10	0.2	1
Cluster Median	-2.07	0.07	53	0.36	0.08	53	0.20	0.12	49	-0.05	0.12	51	0.10	0.13	53
$\log(\epsilon_{\odot})$	7.52			6.36			4.99			6.25			2.13		

In general, we find very good agreement in the atmospheric parameters, radial velocities, and abundances as determined by each study.

The largest discrepancy is seen in the [Ti/Fe] values in the two stars that are in common between this study and Lamb et al. (2015). This is likely due to the low number of Ti I lines

available in our spectral region to constrain the final values. Our measured [Ti/Fe] values, however, are in very good agreement with Mészáros et al. (2015). A full comparison of the 15 stars in our sample in common with Mészáros et al. (2015) is given in a table in the Appendix. Their mean abundances of $\langle[\text{Fe}/\text{H}]\rangle = -1.95 \pm 0.07$ and

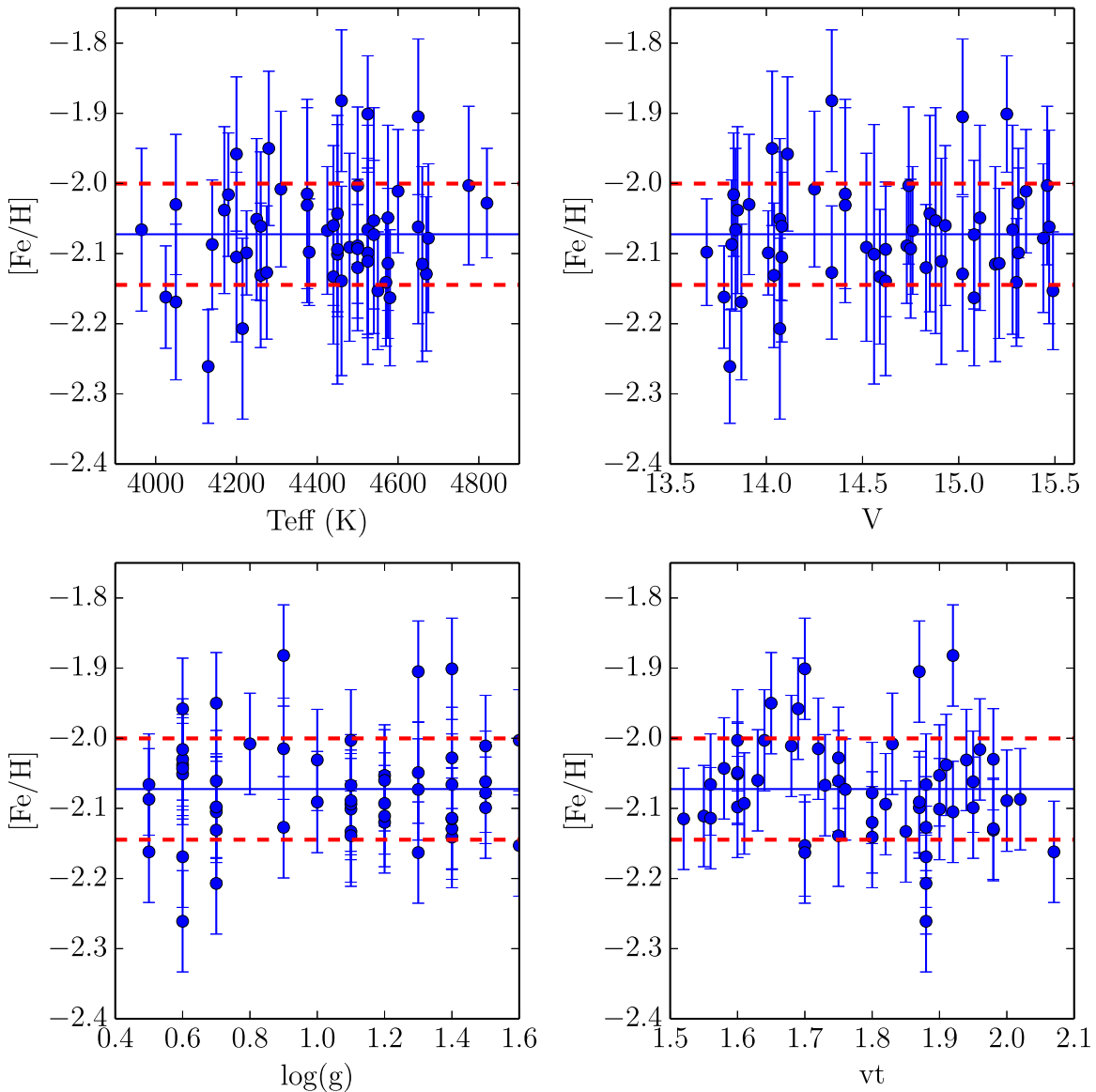


Figure 4. $[\text{Fe}/\text{H}]$ as a function of apparent magnitude V , T_{eff} , $\log(g)$, and v_t . The vertical error bars in each of the plots represent the standard deviation of the $[\text{Fe}/\text{H}]$ abundance of a given star.

$\langle [\text{Ca} + \text{Ti}/2\text{Fe}] \rangle = 0.26 \pm 0.17$ are in agreement with ours. In Table 8 we see that the $[\text{O}/\text{Fe}]$ abundances as measured by Lamb et al. (2015) for stars 51 and 72 are in agreement with our measurements. For each of these stars we were only able to set an upper limit on the $[\text{Na}/\text{Fe}]$ abundances so it is difficult to directly compare their values with ours, although we are in agreement that they are depleted in Na. In this table the Na and O abundances from Lamb et al. (2015) have been placed on our solar scale.

5. DISCUSSION

5.1. Comparison with Milky Way

To put our abundance results in the context of the abundance patterns seen in MW field stars, we plot the $[\text{Ca}/\text{Fe}]$, $[\text{Ti}/\text{Fe}]$, and $[\text{Ba}/\text{Fe}]$ abundances for our M53 cluster stars along with a MW sample taken from Venn et al. (2004) in the right-hand panel of Figure 5. For each species, the individual cluster members of M53 are plotted as open squares and the cluster

median for that species is plotted as a filled star. Also plotted are the average Ca, Ti, and Ba⁴ abundances from our study of NGC 5053. In each cluster the α -element abundances ($[\text{Ca}/\text{Fe}]$ and $[\text{Ti}/\text{Fe}]$), as well as $[\text{Ba}/\text{Fe}]$, are enhanced relative to solar at levels similar to those seen in the MW halo. A recent study by Korotin et al. (2015) calculated a grid of NLTE corrections for $[\text{Ba}/\text{Fe}]$ abundances in cool low metallicity stars. Based on their models for the Ba II line at 6141 Å, the NLTE correction for the stars in our sample would range between -0.1 and -0.25 dex. We have not applied these corrections to the $[\text{Ba}/\text{Fe}]$ abundances presented in this work because our goal was to use them as a comparison to other $[\text{Ba}/\text{Fe}]$ measurements in the literature.

⁴ In our previous study of NGC 5053 we presented a similar figure for the same set of species in that cluster. In that study we reported that the Ba abundance in NGC 5053 is depleted relative to solar with an average value of $[\text{Ba}/\text{Fe}] = -0.54$. In our analysis of M53, we discovered that the hyperfine structure and isotope information in the linelist used in determining Ba was not properly formatted and therefore not properly used by MOOG when creating the synthetic spectra. The corrected values are plotted in Figure 5.

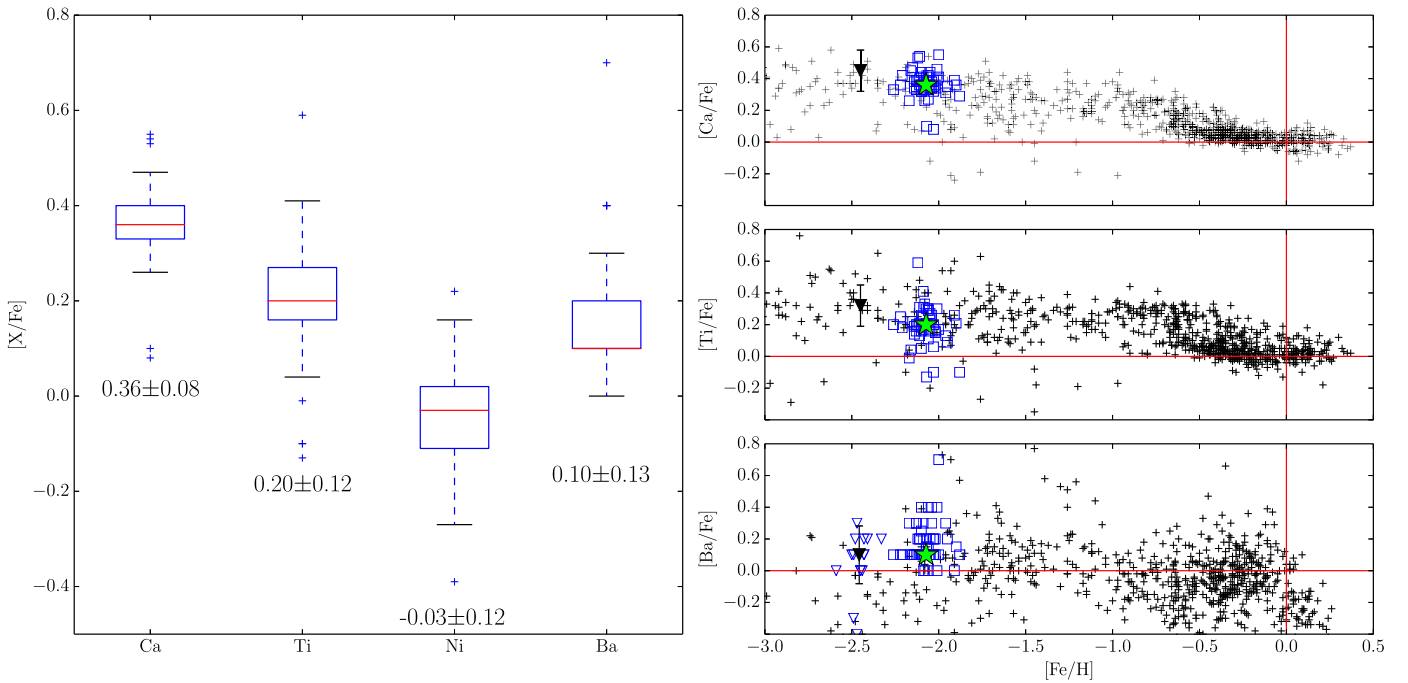


Figure 5. Left panel: box-and-whisker plot of the Ca, Ti, Ni and Ba abundances in M53. The red line is the median of each abundance, the bottom of each box is the 1st quartile (Q1), the top of each box is the 3rd quartile (Q3), and the caps represent the minimum and maximum values. The individual points are outliers defined as being greater or less than $Q3$ or $Q1 \pm 1.5 \times \text{interquartile range (IQR)}$. Right panel: Ca, Ti, and Ba abundances of the stars in our sample plotted with a MW sample taken from Venn et al. (2004), plotted as black crosses. The open squares in each plot represent the individual abundances for each star in our sample, the solid green star marks the median of these individual abundances. The black triangle in each panel marks the median cluster abundance and error in NGC 5053 as measured in our previous study.

Applying these corrections to the MW sample taken from Venn et al. (2004) would be difficult to untangle due to the variety of atmospheric parameters and stellar evolutionary stages represented in the sample.

5.2. Na–O Anti-correlation

In Figure 6 we plot the $[\text{Na}/\text{Fe}]$ versus $[\text{O}/\text{Fe}]$ abundances in M53 as blue filled circles and stars. Those filled markers that are upper limits are plotted with vertical error bars capped with arrows. Plotted with the M53 values, are the Na and O abundances in NGC 7078 and NGC 6809, as measured by Carretta et al. (2009a, 2009b). The abundances taken from these studies have been placed on our assumed solar scale. These clusters were chosen because they are similar in mass and metallicity to M53. Also plotted on the vertical and horizontal axes are the $[\text{Na}/\text{Fe}]$ and $[\text{O}/\text{Fe}]$ histograms for each cluster. From the individual abundances, as well as their histograms, we see that the Na–O anti-correlation in M53 is not nearly as extended as the other two clusters. Specifically, the $[\text{O}/\text{Fe}]$ histogram in M53, plotted in solid blue, has a much shorter tail extending toward oxygen poor values compared to NGC 7078 and NGC 6809. Despite a relatively short O poor tail, the width of the $[\text{O}/\text{Fe}]$ distribution is still wider than is expected based on the measurement errors. The $[\text{O}/\text{Fe}]$ histograms of the three clusters show that the majority of the stars in our sample are slightly more O rich (~ 0.2 dex) than NGC 7078 and NGC 6809. The blue diamond marks the mean $[\text{O}/\text{Fe}]$ value for M53 and the error bars are equal to the standard deviation of our sample. Since the NGC 7078 and NGC 6809 have been placed on our solar scale, we do not have an explanation for this offset. Our $[\text{O}/\text{Fe}]$ abundances,

however, are in agreement with the optical $[\text{O}/\text{Fe}]$ abundances measured by Lamb et al. (2015).

A number of the low $[\text{O}/\text{Fe}]$ stars in NGC 7078 and NGC 6809 are upper limits. Therefore, the O poor tail of each of their distributions could be more extended than these histograms suggest. None of our $[\text{O}/\text{Fe}]$ measurements in M53 are upper limits. The $[\text{Na}/\text{Fe}]$ histogram in M53 is also less extended than in the other two clusters. The extent of the $[\text{Na}/\text{Fe}]$ distribution in M53, however, could be more extended than is shown by the histogram because our lowest $[\text{Na}/\text{Fe}]$ measurements are upper limits. Despite this possible truncation, the $[\text{Na}/\text{Fe}]$ distribution in M53 is still wider than is expected from the errors.

5.3. Population Separation

The division between the FG and SG in $[\text{Na}/\text{Fe}]$ is defined by Carretta et al. (2009b) as $[\text{Na}/\text{Fe}]_{\text{min}} + 4\sigma([\text{Na}/\text{Fe}])$, where $[\text{Na}/\text{Fe}]_{\text{min}}$ is the minimum $[\text{Na}/\text{Fe}]$ abundance in a given cluster as determined by eye from the Na–O anti-correlation, and $\sigma([\text{Na}/\text{Fe}])$ is the typical error on the abundance measurements. This definition is used to characterize the $[\text{Na}/\text{Fe}]$ abundance that is consistent with the Galactic field, and therefore the estimated primordial $[\text{Na}/\text{Fe}]$ abundance of the cluster. As the lowest $[\text{Na}/\text{Fe}]$ measurements in our sample are upper limits, we used the average of the $[\text{Na}/\text{Fe}]$ abundances that divided the populations in NGC 7078 and NGC 6809, as found by Carretta et al. (2009b), to initially split our sample into FG and SG stars. This corresponds to a value of $[\text{Na}/\text{Fe}] = 0.01$ on our assumed solar scale. This value is marked with a dashed magenta line in Figure 6. These clusters were again used because they are similar in mass and metallicity to M53. Using this method results in 30 stars being

Table 7
Na and O Abundances in M53

ID	[Na/Fe]	Error	[O/Fe]	Error
3	0.0	<	0.4	0.1
4	0.4	0.1	0.5	0.1
5	-0.2	<	0.6	0.1
7	0.1	0.1	0.4	0.1
9	-0.1	<	0.4	0.1
10	-0.2	<	0.5	0.1
11	-0.2	<	0.3	0.1
13	0.4	0.1	0.4	0.1
14	0.0	0.2	0.7	0.1
18	0.2	0.1	0.4	0.1
19	0.1	0.1	0.4	0.1
20	-0.2	<	0.5	0.1
24	0.4	0.1	0.2	0.1
25	0.3	0.1	0.2	0.1
27	0.2	0.1	0.5	0.1
28	0.3	0.1	0.3	0.1
29	-0.2	<	0.5	0.1
34	0.4	0.1	0.2	0.1
40	0.0	0.1	0.5	0.1
43	0.1	0.1	0.3	0.1
44	-0.2	<	0.5	0.1
47	0.3	0.2	0.1	0.1
51	-0.2	<	0.6	0.1
53	0.0	0.2	0.3	0.1
54	0.0	<	0.5	0.1
55	0.0	0.1	0.3	0.1
60	0.3	0.1	0.2	0.1
61	0.0	0.1	0.4	0.1
62	0.0	0.1	0.7	0.1
65	-0.1	<	0.4	0.1
68	0.0	<	0.5	0.1
70	0.0	<	0.3	0.2
72	0.0	<	0.3	0.1
78	0.3	0.1	0.5	0.1
80	0.3	0.1	0.4	0.2
85	0.0	<
86	0.0	<	0.5	0.1
88	-0.1	<	0.5	0.1
91	0.1	0.1	0.4	0.1
95	0.2	0.2	0.2	0.2
97	0.0	<	0.1	0.1
101	0.1	<	0.4	0.2
104	0.0	<	0.6	0.2
108	0.3	0.1	0.6	0.1
110	-0.2	<	0.5	0.2
118	0.0	0.2	0.4	0.1
128	-0.2	<
129	0.0	<	0.5	0.1
131	0.0	<

classified as FG stars and 19 stars being classified as SG, or an $N_{\text{SG}}/(N_{\text{SG}} + N_{\text{FG}})$ ratio of 0.39.

Due to the lack of an obvious separation of the FG and SG based solely on the [Na/Fe] abundances and the difficulty of defining a primordial [Na/Fe] in M53, we utilized an additional method to separate and characterize the extent of the populations in the Na–O plane. To do so, we used a two component 2D Gaussian Mixture Model (GMM) over the [Na/Fe] versus [O/Fe] space to classify each star in the sample. This was done utilizing the GMM module from the Python package Scikit-learn (Pedregosa et al. 2011). Each Gaussian component in the GMM was given a full covariance matrix and the expectation-maximization (EM) algorithm was

allowed to run for 1000 iterations. We chose a two component GMM as a means to simultaneously use the [Na/Fe] and [O/Fe] information available for each star when classifying it as a member of the FG or SG. Our data, like most GCs, do not show a clear sign of clumping in the Na–O plane, but rather a smeared out or extended distribution in [Na/Fe]. While this makes it difficult to assign the number of components with algorithms like a GMM, by assuming a two component model, based on our abundance error estimates and the width of the distribution, we are able to use the data to split populations in a situation where it would be difficult to do so by eye.

The center for each of the Gaussian components is plotted as a green circle in Figure 6. The center defining the FG cluster is located at ([O/Fe] = 0.43, [Na/Fe] = -0.03) and the center defining the SG cluster is located at ([O/Fe] = 0.32, [Na/Fe] = 0.31). The separation of the Gaussian components in [Na/Fe] is much larger than the typical errors on the values. The solid red and blue ellipses mark the 1 and 2σ levels of the FG and SG Gaussian components, respectively. Each star is given a probability of belonging to the FG or SG component. A star is classified as FG if its probability of being associated with the FG Gaussian component is $\geq 50\%$. Those stars classified as SG stars by the GMM model are plotted as solid blue stars. In total we find 33 stars with [O/Fe] and [Na/Fe] measurements that are classified as FG stars. Additionally, the 3 stars with only [Na/Fe] measurements are consistent with abundances of the FG sample, so they are also classified as FG, bringing the total to 36. There are 13 stars that are classified as SG stars by the GMM, giving a $N_{\text{SG}}/N_{\text{Total}}$ ratio of 0.27. Comparing this value to what was determined with the Carretta method, $N_{\text{SG}}/N_{\text{Total}} = 0.39$, we see that value of ratio is affected by the method used to separate the populations.

We also applied the GMM technique to separate the populations in NGC 7078 and NGC 6809 based on the abundances available from Carretta et al. (2009a, 2009b). This was done in order to compare the resulting $N_{\text{FG}}/N_{\text{Total}}$ and $N_{\text{SG}}/N_{\text{Total}}$ ratios with the published values in Carretta et al. (2009b). For NGC 6809 the GMM method results in $N_{\text{FG}}/N_{\text{Total}} = 0.38$ and $N_{\text{SG}}/N_{\text{Total}} = 0.62$, while the published values are 0.20 and 0.77, respectively. For NGC 7078 the GMM methods result in $N_{\text{FG}}/N_{\text{Total}} = 0.39$ and $N_{\text{SG}}/N_{\text{Total}} = 0.61$, which matches the published values. This comparison further illustrates how these fractions depend on the method applied. Despite the method used, however, we see that M53 is a GC dominated by the FG, which is in contrast to the majority of GCs which have been found to be dominated by the SG (Carretta et al. 2009b).

We would like to emphasize that the population contributions in M53 could change based on other data, such as photometry. A recent *HST* photometric study on NGC 2808 by Milone et al. (2015) found two photometrically distinct populations in what was designated as the FG in the [Na/Fe] versus [O/Fe] plane (Carretta et al. 2010). As Milone et al. (2015) conclude, this suggests NGC 2808 has undergone a complex stellar evolution, but also highlights the different conclusions that may arise based on the data used to separate the multiple populations.

Bastian & Lardo (2015) find that the published fraction of enriched stars ($f_{\text{enriched}} = N_{\text{enriched}}/N_{\text{total}}$) in 33 MW GCs is very uniform ($f_{\text{enriched}} = 0.68 \pm 0.07$) and does not correlate with initial mass, current mass, metallicity, or current location in the MW. M53 is not included in their sample of 33 GCs, but

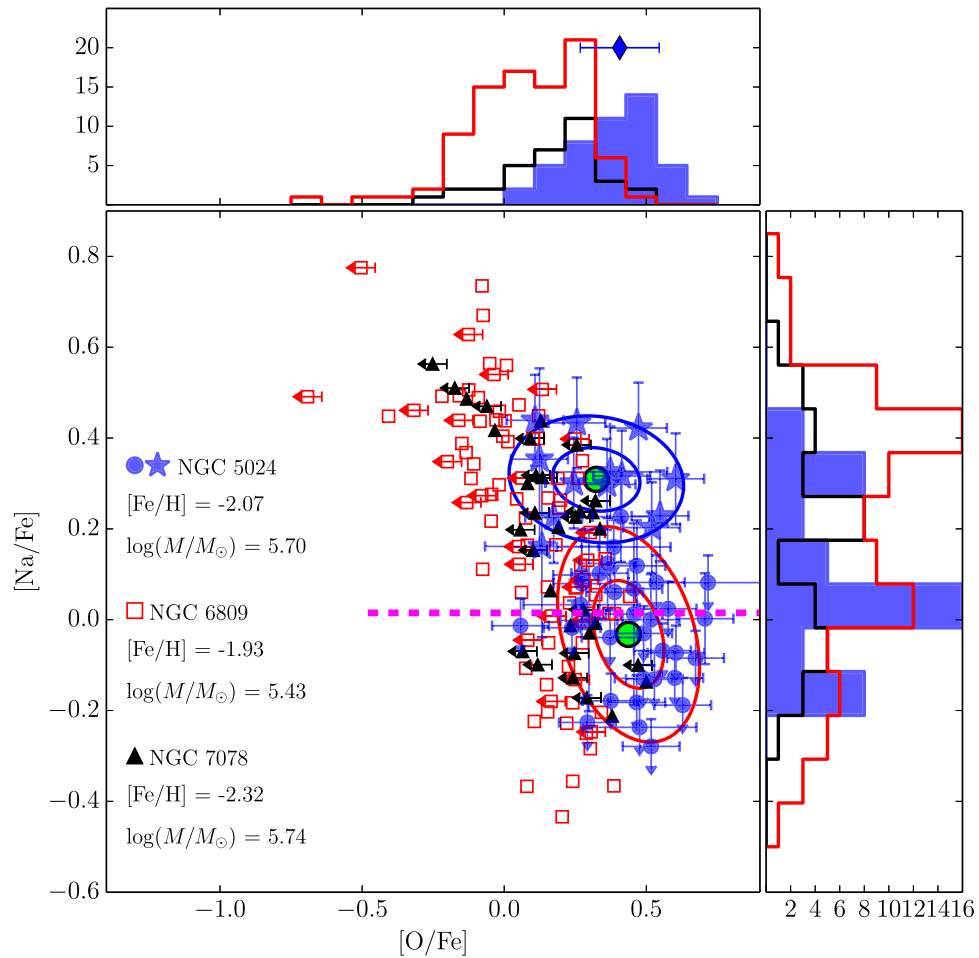


Figure 6. Plot of $[\text{Na}/\text{Fe}]$ vs. $[\text{O}/\text{Fe}]$ abundances in M53 (NGC 5024), NGC 6809, and NGC 7078. The $[\text{Fe}/\text{H}]$ abundance and mass for each cluster is indicated. The data points for M53 have been slightly shifted from the values listed in Table 7 so the total number of stars in our sample is visible. The $[\text{Na}/\text{Fe}]$ and $[\text{O}/\text{Fe}]$ histograms match the color coding for each cluster's marker. The green circles mark the centers of the 2 Gaussian components resulting from generating the GMM. The ellipses mark the 1 and 2σ levels of each Gaussian component. The dashed magenta line marks the $[\text{Na}/\text{Fe}]$ abundance used to separate the FG and SG using the Carretta method.

Table 8
Comparison with Lamb et al. (2015) and Mészáros et al. (2015)

Lamb ID Hydra ID 2MASSID	RV (km s^{-1})	$\log(g)$ (cm s^{-2})	T_{eff} (K)	v_t (km s^{-1})	$[\text{Fe}/\text{H}]$	$[\text{Ca}/\text{Fe}]$	$[\text{Ti}/\text{Fe}]$	$[\text{Ba II}/\text{Fe}]$	$[\text{Na}/\text{Fe}]$	$[\text{O}/\text{Fe}]$
5024-22254	-58.40	1.21	4410	1.60	-2.17	0.31	-0.14	0.17	-0.47	0.50
72	-57.56	1.20	4540	1.90	-2.05	0.34	0.27	0.10	<0.0	0.30
13124794+1806320	-55.1	1.11	4564	...	-1.99	0.19	0.29
5024-50371	-62.10	1.06	4444	1.80	-2.15	0.26	-0.09	0.25	-0.67	0.65
51	-62.69	1.10	4450	1.90	-2.10	0.32	0.16	0.25	<-0.2	0.60
13131736+1814463	-61.5	1.15	4583	...	-1.94	-0.01

based on our findings, would have $f_{\text{enriched}} = 0.27$ based on the GMM method, or $f_{\text{enriched}} = 0.39$ based on the Carretta method. In either case, these values are well outside the mean value and scatter found by Bastian & Lardo (2015) and further highlight how M53 is different from the majority of GCs based on its $[\text{Na}/\text{Fe}]$ and $[\text{O}/\text{Fe}]$ abundances.

5.4. Radial Distributions of FG and SG

With the stars classified as FG and SG we are able to produce the cumulative distribution of the radial distance from the cluster center for each population. These distributions are plotted in Figure 7 as red and blue lines for the FG and SG,

respectively. Over the radii covered by the stars in our sample, we see that the SG is more centrally concentrated than the FG and still retains some memory of the SG spatial segregation predicted by the multiple-population formation models discussed in the introduction.

5.5. Comparison with CN and CH Molecular Band Strengths

A previous study by Martell et al. (2008) used the distributions of CN and CH molecular band strengths as a method to characterize multiple populations in M53. As noted by the authors, M53 is near the low end of the metallicity spectrum where the CN band strength distribution shows a

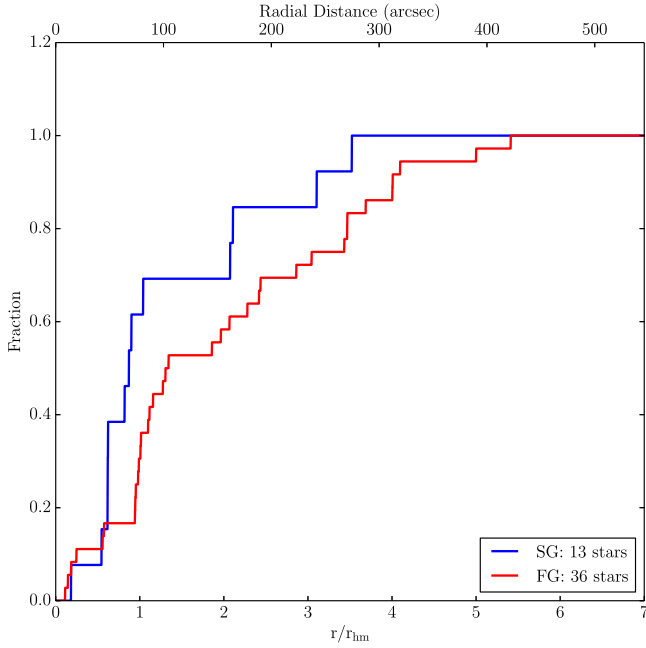


Figure 7. Cumulative radial distributions for the FG and SG stars as defined by the GMM.

bimodal shape, indicating the presence of multiple populations. Below $[\text{Fe}/\text{H}] \sim -2.1$, the CN band becomes insensitive to changes in N so that clusters of low metallicity, with multiple populations seen in Na–O, do not show a range of CN strengths. The authors find that the CN distribution in M53 is not bimodal, but is much wider (3σ) than the errors on the measurements. Based on the narrow range of C and N in M53, Martell et al. (2008) conclude that the polluting material from the FG had not been fully processed through the CNO cycle. This would suggest that O has not been converted to N, the NeNa cycle has not been activated, and therefore M53 should not show a Na–O anti-correlation. With our data we are able to determine how the Na-enhancement in M53 correlates with the

CN strengths measured by Martell et al. (2008). Due to the relationship between the CNO and the NeNa cycle, the CN strong stars are expected to have a one-to-one correlation with the Na-enhanced stars in the cluster, as has been shown in a number of GCs (Gratton et al. 2012).

In the left-hand panel of Figure 8 we plot the distribution of CN band strengths as measured by Martell et al. (2008). In the right-hand panel of Figure 8 we plot $[\text{Na}/\text{Fe}]$ versus $[\text{O}/\text{Fe}]$ for our sample of M53 stars and color code the stars in common with that study by their CN band strength. The ellipses once again mark the 1 and 2σ levels of the FG and SG Gaussian components. From the right-hand panel of Figure 8, we see that while the most Na-enhanced stars are indeed CN-strong, not all the CN-strong stars are Na-enhanced, and some look Na-normal. This suggests that there is not a completely one-to-one relationship between the CN band strength and Na abundance in M53, and there is a range of CN strength at a given Na abundance. A similar result has also been found in M5 and 47 Tuc by Smith et al. (2013) and Smith (2015), respectively. In these studies, the CN strength in RGB stars did not show a completely one-to-one correlation with $[\text{Na}/\text{Fe}]$. Smith et al. (2013) suggest that the initial enhancement, or lack thereof, in Na does not necessarily go in step with the N abundance needed to produce the signature of a CN-normal or CN-strong star. This further illustrates how one can reach different conclusions about the contributions of multiple populations in GCs based on the data used to separate them.

There are also molecular band strength measurements in M53 from Smolinski et al. (2011). While we do not have stars in common with that study, the authors combined their sample with that of Martell et al. (2008) to better characterize the CN band strength distribution in M53. The CN distribution created from the combined dataset more clearly shows the presence of a CN-normal and CN-strong population. They also find that the ratio of CN-strong to CN-weak stars is 0.61, which would indicate a majority of FG stars in the cluster. This fraction, however, is derived from a relatively small number of stars, and as stated earlier, the CN strength does not necessarily trace the multiple populations as defined by the Na–O anti-correlation.

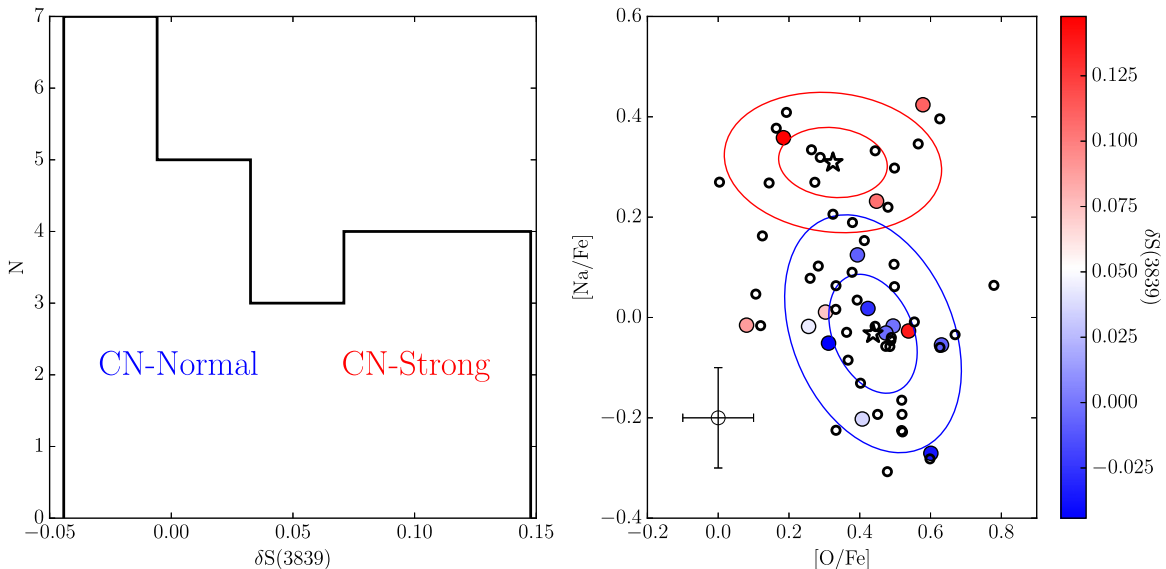


Figure 8. Left panel: histogram of CN molecular band strengths in M53 RGB stars from Martell et al. (2008). Right panel: plot of $[\text{Na}/\text{Fe}]$ vs. $[\text{O}/\text{Fe}]$ abundances in M53. The stars from Martell et al. (2008) in common with our study are color coded according to their molecular band strength. The open circle with error bars in the lower-left-hand corner shows our typical errors in Na and O measurements.

Smolinski et al. (2011) also note that the CN and CH band strengths in their M53 sample are uncorrelated, which is in contrast to the anti-correlation between these band strengths that is typically observed in GCs. This is another indication of the unique chemical signatures in M53.

6. CONCLUSIONS

From a large sample of RGB stars in M53, we find Fe, Ca, Ti, Ni, and Ba abundances consistent with other published results, and the trends seen in MW halo stars. We find that M53 has an Na–O anti-correlation that is not as extended as other MW GCs of similar mass and metallicity. The ratio of $N_{\text{SG}}/N_{\text{Total}}$ in the cluster is approximately 0.3, making M53 a FG-dominated cluster as predicted by Caloi & D’Antona (2011) on the basis of simulations of its HB morphology. The SG stars in our sample are more concentrated in the cluster central regions and retain some memory of the initial SG segregation predicted by multiple-population formation models. By comparing the Na–O anti-correlation in M53 with previously available molecular band strength measurements, we see that there is not a one-to-one correlation between the CN-strong and the Na-enhanced populations. Specifically, we find that a few CN-strong stars are not enhanced in Na; this finding suggests that some stars belonging to the SG population, as classified by their CN strengths (CN-strong), might be found in the FG region of the Na–O plane (see D’Antona et al. 2016 for a possible model explaining the origin of stars with these chemical properties). This is important to consider when drawing conclusions about the chemical

characteristics of the multiple populations in GCs, and the interplay between the strength of the CN molecular features and the enhancement of Na.

Using the individual radial velocities we measured we will characterize the internal rotation of M53 using the methods similar to those shown in Bellazzini et al. (2012), Bianchini et al. (2013), and Kacharov et al. (2014). Measuring the amplitude of the rotation in the cluster, and its velocity dispersion profile, will allow us to compare our observations to theoretical models through N -body simulations. These comparisons will allow us to explore how the morphological features of M53, such as ellipticity, are affected by the internal dynamics of the cluster. This kinematic study will be an additional piece of our comprehensive study of M53 and NGC 5053.

This material is based on work supported by the National Science Foundation Graduate Research Fellowship Program under Grant No. DGE-1342962 to OB. Any opinion, findings, and conclusions or recommendations expressed in this material are those of the author(s) and do not necessarily reflect the views of the National Science Foundation. E.V. acknowledges support from grant NASA-NNX13AF45G. We would also like to acknowledge the use of the 2MASS point source catalog for completing this research.

APPENDIX

The table in this appendix (Table 9) provides a full abundance comparison of the 15 stars in our sample in common with Mészáros et al. (2015).

Table 9
Comparison with APOGEE sample

2MASSID	RV	log(g)	T_{eff}	[Fe/H]	[Ca/Fe]	[Ti/Fe]
13125038+1814391	−60.0	1.27	4648	−1.97	0.28	0.27
111	−63.8
13125496+1805350	−63.6	1.48	4734	−1.98	0.44	0.16
86	−65.4	1.40	4670	−2.13	0.39	...
13125650+1812375	−58.9	1.11	4570	−2.12	0.40	0.39
97	−60.3	1.40	4575	−2.11	0.54	0.21
13123617+1807320	−56.5	1.02	4505	−1.96	0.51	0.40
65	−57.2	1.20	4425	−2.07	0.39	0.30
13123737+1808232	−57.6	0.48	4229	−1.87	0.20	0.13
27	−60.1	0.70	4200	−2.11	0.36	0.13
13124552+1811289	−61.9	0.48	4206	−1.88	0.14	0.21
4	−61.3	0.70	4050	−2.22	0.36	0.26
13124768+1810060	−68.3	0.96	4496	−1.88	0.20	0.27
39	−69.7	0.80	4460	−1.88	0.29	−0.10
13124794+1806320	−55.1	1.11	4564	−1.99	0.19	0.29
72	−58.4	1.20	4540	−2.05	0.34	0.27
13124819+1812465	−61.7	1.06	4534	−1.86	−0.12	0.46
53	−62.8	1.10	4440	−2.13	0.33	0.19
13124987+1811487	−56.6	1.33	4682	−2.04	0.02	0.42
87	−59.3	1.30	4580	−2.16	0.45	0.04
13125725+1806050	−61.8	1.23	4613	−1.89	0.23	0.42
60	−62.2	1.10	4500	−2.09	0.34	0.41
13130246+1813234	−60.7	1.19	4598.0	−2.01	0.34	−0.02
68	−61.1	1.20	4500.0	−2.12	0.39	0.20
13130442+1808556	−59.1	1.11	4564.0	−1.93	0.35	0.22
99	−60.8
13130531+1814508	−65.6	1.33	4670.0	−1.92	0.26	...
54	−65.8	1.10	4460.0	−2.14	0.38	0.14
13131736+1814463	−61.5	1.15	4583.0	−1.94	−0.01	...
51	−62.1	1.10	4450.0	−2.10	0.32	0.16

REFERENCES

- Alonso, A., Arribas, S., & Martínez-Roger, C. 1999, *A&AS*, **140**, 261
- Anders, E., & Grevesse, N. 1989, *GeCoA*, **53**, 197
- Bastian, N., Lamers, H. J. G. L. M., de Mink, S. E., et al. 2013, *MNRAS*, **436**, 2398
- Bastian, N., & Lardo, C. 2015, *MNRAS*, **453**, 357
- Bellazzini, M., Bragaglia, A., Carretta, E., et al. 2012, *A&A*, **538**, A18
- Bianchini, P., Varri, A. L., Bertin, G., & Zocchi, A. 2013, *ApJ*, **772**, 67
- Boberg, O. M., Friel, E. D., & Vesperini, E. 2015, *ApJ*, **804**, 109
- Caloi, V., & D'Antona, F. 2011, *MNRAS*, **417**, 228
- Carretta, E., Bragaglia, A., Gratton, R., & Lucatello, S. 2009a, *A&A*, **505**, 139
- Carretta, E., Bragaglia, A., Gratton, R. G., et al. 2009b, *A&A*, **505**, 117
- Carretta, E., Bragaglia, A., Gratton, R. G., et al. 2010, *A&A*, **516**, A55
- Carretta, E., Bragaglia, A., Gratton, R. G., & Tosi, M. 2004, *A&A*, **422**, 951
- Chun, S.-H., Kim, J.-W., Sohn, S. T., et al. 2010, *AJ*, **139**, 606
- D'Antona, F., Vesperini, E., D'Ercole, A., et al. 2016, *MNRAS*, **458**, 2122
- Decressin, T., Baumgardt, H., Charbonnel, C., & Kroupa, P. 2010, *A&A*, **516**, A73
- de Mink, S. E., Pols, O. R., Langer, N., & Izzard, R. G. 2009, *A&A*, **507**, L1
- D'Ercole, A., D'Antona, F., Carini, R., Vesperini, E., & Ventura, P. 2012, *MNRAS*, **423**, 1521
- D'Ercole, A., D'Antona, F., Ventura, P., Vesperini, E., & McMillan, S. L. W. 2010, *MNRAS*, **407**, 854
- D'Ercole, A., Vesperini, E., D'Antona, F., McMillan, S. L. W., & Recchi, S. 2008, *MNRAS*, **391**, 825
- Gratton, R. G., Carretta, E., & Bragaglia, A. 2012, *A&ARv*, **20**, 50
- Gustafsson, B., Edvardsson, B., Eriksson, K., et al. 2008, *A&A*, **486**, 951
- Harris, W. E. 1996, *AJ*, **112**, 1487
- Heiter, U., Lind, K., Asplund, M., et al. 2015, *PhyS*, **90**, 054010
- Johnson, C. I., Pilachowski, C. A., Simmerer, J., & Schwenk, D. 2008, *ApJ*, **681**, 1505
- Jordi, K., & Grebel, E. K. 2010, *A&A*, **522**, A71
- Kacharov, N., Bianchini, P., Koch, A., et al. 2014, *A&A*, **567**, A69
- Kimmig, B., Seth, A., Ivans, I. I., et al. 2015, *AJ*, **149**, 53
- Korotin, S. A., Andrievsky, S. M., Hansen, C. J., et al. 2015, *A&A*, **581**, A70
- Lamb, M. P., Venn, K. A., Shetrone, M. D., Sakari, C. M., & Pritzl, B. J. 2015, *MNRAS*, **448**, 42
- Lind, K., Asplund, M., Barklem, P. S., & Belyaev, A. K. 2011, *A&A*, **528**, A103
- Martell, S. L., Smith, G. H., & Briley, M. M. 2008, *PASP*, **120**, 7
- McLaughlin, D. E., & van der Marel, R. P. 2005, *ApJS*, **161**, 304
- McWilliam, A. 1998, *AJ*, **115**, 1640
- Mészáros, S., Martell, S. L., Shetrone, M., et al. 2015, *AJ*, **149**, 153
- Milone, A. P., Marino, A. F., Piotto, G., et al. 2015, *ApJ*, **808**, 51
- Pedregosa, F., Varoquaux, G., Gramfort, A., et al. 2011, *J. Mach. Learn. Res.*, **12**, 2825
- Pilachowski, C. A., Sneden, C., & Kraft, R. P. 1996, *AJ*, **111**, 1689
- Piotto, G., Milone, A. P., Bedin, L. R., et al. 2015, *AJ*, **149**, 91
- Prantzos, N., & Charbonnel, C. 2006, *A&A*, **458**, 135
- Rey, S.-C., Lee, Y.-W., Byun, Y.-I., & Chun, M.-S. 1998, *AJ*, **116**, 1775
- Rieke, G. H., & Lebofsky, M. J. 1985, *ApJ*, **288**, 618
- Skrutskie, M. F., Cutri, R. M., Stiening, R., et al. 2006, *AJ*, **131**, 1163
- Smith, G. H. 2015, *PASP*, **127**, 825
- Smith, G. H., Modi, P. N., & Hamren, K. 2013, *PASP*, **125**, 1287
- Smolinski, J. P., Martell, S. L., Beers, T. C., & Lee, Y. S. 2011, *AJ*, **142**, 126
- Sneden, C. 1973, *ApJ*, **184**, 839
- Sousa, S. G., Santos, N. C., Adibekyan, V., Delgado-Mena, E., & Israelian, G. 2015, *A&A*, **577**, A67
- van Dokkum, P. G. 2001, *PASP*, **113**, 1420
- Venn, K. A., Irwin, M., Shetrone, M. D., et al. 2004, *AJ*, **128**, 1177
- Ventura, P., D'Antona, F., Mazzitelli, I., & Gratton, R. 2001, *ApJL*, **550**, L65
- Wallace, L., Hinkle, K. H., Livingston, W. C., & Davis, S. P. 2011, *ApJS*, **195**, 6